



Quantitative Study of Residual Strain and Geometrically Necessary Dislocation Density Using HR-EBSD Method

C. Zhao^{1,2,3} · X. Li^{1,2}

Received: 1 October 2020 / Accepted: 27 May 2021 / Published online: 17 August 2021
© Society for Experimental Mechanics 2021

Abstract

Background Optical metrology is widely used to measure materials' deformation and mechanical properties but current fundamental research requires more precise measurement of microstructure and deformation in internal materials. Electron backscattered diffraction (EBSD) technique measures crystal orientation in individual grain and high resolution EBSD (HR-EBSD) method provides information about residual strain and GND density.

Objective Deformation of two stainless steels Nitronic 60 and Tristelle 5183 with different proportions of ferrite and carbides are characterised.

Methods Push-release bend testing was used to provide progressive increasing bending stress in two iron-based material samples. HR-EBSD and high resolution digital image correlation (HR-DIC) methods characterised residual strain, GND density and plastic strain distributions in each sample.

Results Nitronic 60 and Tristelle 5183 were deformed and obtained 3.8% and 0.9% plastic strain ϵ_{xx} . High GND densities distributed neighbouring grain boundaries in Nitronic 60 while high GND densities distributed around carbides, especially intragranular carbides in Tristelle 5183.

Conclusions HR-EBSD and HR-DIC quantitative characterised deformation in two iron-based alloys, grain/twin boundaries and carbides resulted in GND density increase, promoted work hardening and accumulated high residual elastic strain. Heterogeneous grain/carbide size distribution led to stress concentration and cause carbide decohesion and brittle fracture of sample.

Keywords EBSD · Residual strain · GND · DIC

Introduction

Optical metrology provides full field, noncontact, precise measurement of various physical parameters of materials, structures, and devices. These properties include kinematic parameters (displacement, velocity, and acceleration), deformation parameters (strain, curvature, and twist), surface parameters (shape and roughness), and mechanical properties of materials (Young's modulus, Poisson's ratio, etc.). Researchers have developed many delicate optical

measurement techniques and methods, such as photoelasticity, holographic interferometry, speckle metrology, Moiré methods, fibre sensing, laser Doppler vibrometry and velocimetry, and computer-vision-based techniques [1–4]. However, new requirements arise with the recent development in fundamental research and industry applications to fulfill non-destructive and precise measurement in internal materials/structures or related to the microstructure of the materials, which lead to the introduction of spectroscopy and radiation technique into the characterization and measurement of mechanical properties of materials. These technologies include Raman spectroscopy, infrared spectroscopy, high energy X-ray, terahertz, neutron diffraction, and synchrotron radiation.

Raman spectroscopy commonly uses monochromatic visible light and as incident source to observe inelastic scattering of photons then analyse matter's structure and vibrational modes [5, 6]. It has single molecular level resolution and can analyse chemical composition and structures in

✉ X. Li
lixide@tsinghua.edu.cn

¹ Department of Engineering Mechanics, Tsinghua University, Beijing 100084, China

² Center for Nano and Micro Mechanics, Tsinghua University, Beijing 100084, China

³ Department of Materials, Imperial College London, Exhibition Road, London SW7 2AZ, UK



different types of materials [7–13]. Infrared spectroscopy is another classical structure determination technique which uses absorbance and transmittance of infrared ray to identify chemical compositions and structures in materials like metal, protein and graphene [14–18]. High frequency electromagnetic radiation such as x-ray, terahertz waves were also utilised in specific spectroscopies to investigate chemical compositions and crystal structures in metals, semiconductors and biomaterials [19–24]. High-energy neutrons are utilized in neutron diffraction spectroscopy which can determine crystalline structure and quantitatively measure residual stress tensor in metals [25–31]. Synchrotron radiation provides spectroscopies unprecedented induce beams with advantages such as high brilliance, high flux and accurate frequency [32–34].

Electron Back Scatter Diffraction (EBSD), which uses electrons as incidence source, is utilized to examine the crystal orientation at each individual scanning point to provide information of phase, grain size, grain boundaries, crystal orientation and misorientation in different types of materials from several microns to millimetres [35]. Backscattered electrons diffract when their incidence angles satisfy Bragg equation:

$$n\lambda = 2d\sin\theta \quad (1)$$

where n is an integer, λ is the wavelength of electrons, d is spacing of atomic planes and θ is angle between incident electrons and diffracting planes. For individual point in testing sample, backscattered electrons satisfying Bragg's equation are diffracted then received by a charge-coupled device (CCD) detector to form Kikuchi patterns [36]. Kikuchi patterns are transferred into specific dots in Hough space and interpreting the processed Kikuchi patterns give the exact orientation of each point [37, 38]. As shown in Fig. 1(a), (b), the red lines in Kikuchi patterns corresponding to diffracting planes so each Kikuchi band can be indexed by Miller indices and the exact orientation can be calculated.

High angular resolution EBSD (HR-EBSD) is based on conventional EBSD equipment to obtain high-quality

electron beam scattering patterns then the lattice curvature components are calculated by measuring relative pattern movements between testing patterns and reference pattern in each grain [39]. Similar as those non-destructive residual stress measurement techniques such as Neutron Diffraction and X-Ray Diffraction, EBSD can measure crystal lattice spacing change to calculate deviatoric elastic strain gradient and rigid body rotations to determine surface residual stress in crystalline materials. HR-EBSD technique carries out correlation between two or more EBSD patterns with a sensitivity of 1×10^{-4} in strain and 1×10^{-4} rad in rotation [40]. The elastic strain and rotation about three orthogonal axes on the sample surface measured by this method with $\times 100$ improvement in angular resolution comparing to conventional Hough based EBSD technique. HR-EBSD calculates six lattice rotation curvature components which provide dislocation densities based on an energy minimization scheme then giving geometrically necessary dislocation densities (GND), which obtained accurate results on titanium alloy and copper alloy [41, 42]. Wilkinson et al. utilized HR-EBSD in measuring lattice curvature and GND density in a fatigue crack growth process to analyse material's fatigue crack behaviour [39]. The HR-EBSD method measure lattice curvature such that when combined with the Nye tensor decomposition, it allows for the extraction of GND density and small step size is used to get most accurate dislocation density [43]. Statistic stored dislocations (SSD) occur in dipoles or multipoles but do not give rise to a net open Burgers vector. Measuring SSD density is difficult requiring other techniques which only allow for an estimate to be established and it is immeasurable by HR-EBSD [44]. Elastic and plastic strain accumulation is measured and micro-crack nucleation is observed by HR-EBSD and high resolution digital image correlation (HR-DIC) in a nickel alloy [45] and similar method is applied on a dual-phase steel [46].

In this study, HR-EBSD and HR-DIC will be utilized to measure elastic/plastic strain and GND density accumulation before and after deformation to study microstructures and reinforcement phases' influence in deformation of two iron-based materials.

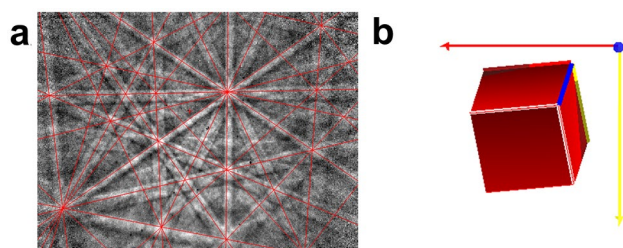


Fig. 1 Kikuchi patterns for EBSD analysis. (a) crystal planes corresponding to Kikuchi bands; (b) simulated crystal orientation by interpreting Kikuchi patterns

Materials and Methods

Materials

Two stainless steels Nitronic 60 and Tristelle 5183 are studied in this paper and the two alloys are designed for excellent wear and corrosion resistance [47, 48]. Their mechanical properties are listed in Table 1 and stress–strain curves are shown in Fig. 2.



Table 1 Mechanical properties of each tested material [49]

Material	Young's Modulus/ GPa	Yield strength/ MPa	Ultimate Tensile Strength/ MPa	Elongation	Hardness/ HV10
Nitronic 60	180	414	800	70%	218
Tristelle 5183	210	710	1102	2%	421

Casted Nitronic 60 was extruded to round bar shape then annealed at 955 °C, a large number of twins was formed due to its low stacking fault energy [47]. Nitronic 60 is much ductile than Tristelle 5183 and its elongation rate is up to 70% and the ultimate tensile strength is 800 MPa. Tristelle 5183 has larger fraction of carbides and higher hardness [50], it was formed by hot isostatic pressing (HIP) powder metallurgy which significantly reduced the grain size, elevated its yield stress and ultimate strength than conventional cast form [51].

Sample Preparation and EBSD Characterisation

Materials were machined into samples with dimensions of 3 mm × 3 mm × 12 mm for three-point bend testing. Each sample's surface of interest was firstly ground on a Struers RotoPol21 grinding machine at 200r/min with a series of grit silicon carbide papers (#800 for 2 min, #1200 for 3 min, #2000 for 4 min and #4000 for 5 min). After all grinding steps, samples were polished on a Struers Tegramin polishing machine with 1 μm diamond suspension for 10 min then finally polished for 10 min using 50 nm colloidal silica suspension.

Polished samples were characterized in a Zeiss Auriga scanning electronic microscopy (SEM) which equipped Bruker QUANTAX EBSD detector. The middle-lower area

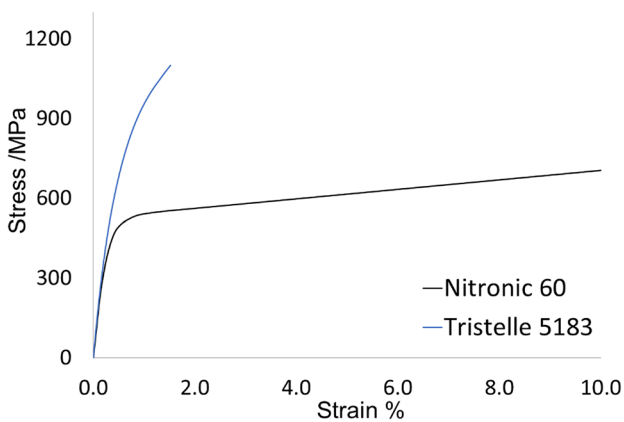


Fig. 2 Stress–strain curves for the two testing materials [49]

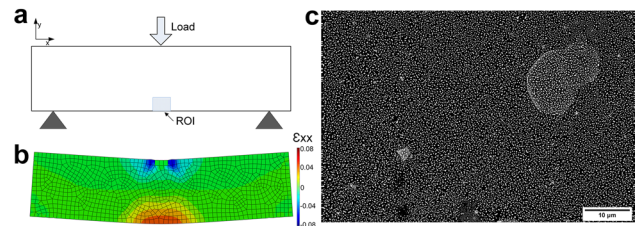


Fig. 3 Design of three-point bend testing and gold speckles for HR-DIC. (a) schematic diagram of a sample under three-point bend test (blue dashed region indicates the ROI where HR-DIC and HR-EBSD were carried out), (b) finite element analysis of model beam strain ϵ_{xx} developed at peak loading with representative Nitronic 60 elastic–plastic properties; (c) gold speckles captured by 4000× magnification BSE microscope (white spots: gold particles, dark: areas not covered by gold) [49]

of each sample's front surface (in few microns) where has highest tensile stress was select as region of interest (ROI). Sample was tilted 70° from horizontal for EBSD characterization with 20 kV acceleration voltage, probe current of 2nA and 15 mm working distance. The electron beam scattering patterns were collected by EBSD detector for conventional EBSD analysis to obtain phase and grain orientation maps. These saved patterns were saved for subsequent HR-EBSD analysis to calculate surface quantitative information including GND density, residual elastic strains.

Three-point Bend Testing and HR-DIC Analysis

Ex-situ three-point bend testing was carried out on each sample with gold speckles. As schematic diagram Fig. 3(a) shows, this push-release test was carried on a Zwick Roell mechanical testing machine equipped with three-point bending rig. Under three-point bending condition, the shear effects can be neglected as they are anticipated to be very small near the beam bottom free surface and the ROI is sufficiently small with respect to the 3 mm × 3 mm × 12 mm beam, it is reasonable to consider this method provides a uniform x-direction tensile stress state in ROI.

According to Table 2, four increasing amplitude loads were applied on each sample and backscattered electron (BSE) images were captured before and after each load for

Table 2 Progressive loading history for different materials. The stresses shown correspond to the peak stress σ_{xx} at ROI

Materials	Applied force/ Simulated stress σ_{xx}				Simulated ϵ_{xx}
	1st load	2nd load	3rd load	4th load	
Nitronic 60	1550 N/ 566 MPa	1700 N/ 579 MPa	1850 N/ 609 MPa	2000 N/ 633 MPa	7%
Tristelle 5183	2700 N/ 1075 MPa	2900 N/ 1138 MPa	3100 N/ 1150 MPa	3300 N/ 1153 MPa	2%



HR-DIC analysis. Progressive bending stress profile is listed in Table 2 and the loading rate was set as 50 N/s for all tests. Conventional finite element simulation was carried out with representative elastic–plastic properties of each material to determine corresponding applied load for estimated total strain ϵ_{xx} and one example was shown in Fig. 3(b). Due to the different ductility of Nitronic 60 and Tristelle 5183, the estimated final total strain ϵ_{xx} of ROI were set as 7% and 2% respectively and the applied loads were correspondingly determined.

Digital Image Correlation (DIC) is a quantitatively deformation measuring technique which compares two or more digital photos of the same sample at different stages of deformation to calculate strain, rotation and displacement [52]. Random fine distributed speckles are added on the surface of interest to obtain accurate displacement components at ROIs. Speckle patterns of the deformed samples are numerically correlated with the reference samples then the local object displacement vector can be calculated. High resolution DIC (HR-DIC) works at high magnification that measures strain below grain scale. As Fig. 3(c) shows, a 25 nm thin layer of gold speckles was formed on each sample by gold remodelling method to obtain accurate HR-DIC deformation measurement and Sub-micron sized gold speckles had been achieved over the sample ROI [49]. The large difference of element mass between gold and testing materials gives a clear contrast between gold speckles and sample base. The progressive bend testing method creates increasing stress states so the gradually increased strain distribution in ROI during the bending process can be obtained by HR-DIC method. After finishing all tests, sample was gently re-polished by OP-S colloidal silica suspension for 3 s to remove gold speckles after the three-point bend testing. The polished samples were then taken for EBSD characterization on the same ROI. The re-polishing time was very short and the normal contact force was only a few mN, considering the high yield stress of the two alloy, it is reasonable to argue the re-polishing process has neglectable effect on following HR-EBSD analysis.

Results

Nitronic 60

The extruded Nitronic 60 has a coarse grain size so 1500 \times magnification was used to apply EBSD and HR-DIC measurements. In the preliminary SEM observation, a small volume fraction of ferritic phase was found in the form of elongated stringers along the extrusion direction (extrusion direction labelled in Fig. 4). Nitronic 60 sample with ferrite stringers perpendicular to the tensile bending direction was chosen to illustrate stress–strain distributions in austenite

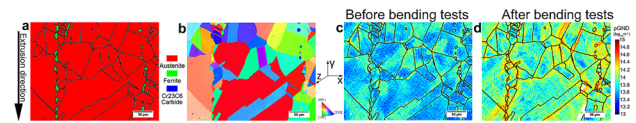


Fig. 4 Results obtained for Nitronic 60 sample showing (a) phase map, (b) EBSD orientation maps before test, (c) and (d) HR-EBSD GND density maps before and after bend testing

and ferrite before and after bend testing. EBSD orientation and HR-EBSD results for Nitronic 60 sample are presented in Fig. 4.

According to Fig. 4(a), Nitronic 60 is mainly constituted by austenite (area fraction over 96%), with a small proportion of ferrite and tiny content of chromium carbide particles. Grains of austenite and ferrite can be observed in Fig. 4(b), in which the average grain size of austenite is clearly much larger than that for ferrite, with some extremes for the austenite phase. Grain size of austenite in Nitronic 60 sample is around 50 μm which is much higher than that of ferrite. The material is extruded and annealed so EBSD scanning shows significant twinning in austenite phase.

HR-EBSD technique compares two or more EBSD patterns to calculate six lattice rotation curvature components then calculates geometrically necessary dislocation densities (GND) based on an energy minimization scheme [41, 42]. An increase of GND density is observed from Fig. 4(c), (d) which indicates considerable development of inter-granular straining and hence distortion during the deformation. GND density near grain boundaries is distinctly higher than in the bulk of the grains. Higher GND densities are also observed at many ferrite–austenite phase boundaries, and within the small ferrite regions themselves.

Figure 5 shows the residual elastic strain maps determined by HR-EBSD. HR-EBSD technique selects a reference pattern (typically the pattern with best quality) in each grain then calculates elastic strain by measuring relative pattern movements between testing patterns and selected reference pattern [39]. Due to the reference selection scheme limit, only intragranular relative elastic strain values are attainable while intergranular residual strains are not comparable, i.e. the residual strain maps show relative strain values but not absolute values. It is notable after bending test within some grains, the relative elastic residual strain increased distinctly

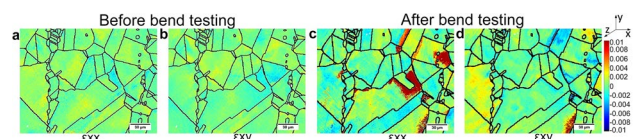


Fig. 5 HR-EBSD elastic residual strain ϵ_{xx} and ϵ_{xy} maps for Nitronic 60 sample showing (a) and (b) before bend testing; (c) and (d) after bend testing



to 1%. The residual normal and shear strain distribution is very heterogeneous, regions with high GND densities commonly have high relative residual strains and high residual strain commonly occurred at grain boundaries.

HR-DIC calculated total strain ϵ_{xx} development during progressive cyclic loading are shown in Fig. 6(a)–(d). Apparent Schmid factor shown in Fig. 6(e) was calculated using loading direction of x-direction.

The ϵ_{xx} obtained from the HR-DIC measurements is again very heterogeneous, with some grains showing early slip activation and strain developed rapidly. Localized bands of persistent slip are observed to develop within the central region, for about 45° to the bending direction. As calculation from Fig. 4(b), twin boundaries constitute $\sim 50\%$ total length of all boundaries. The existence of twinning boundary led to dislocation accumulation and slip transfer inhibition and the large amount of twinning effectively reduced the average grain size which enhanced material’s yield stress. Ferrite phase grains remain largely undeformed in the ϵ_{xx} maps, suggesting that the ferrite phase in this material has higher slip strength and is harder to be deformed.

On comparing the HR-DIC result with Schmid factor map, grains with high Schmid factors commonly show relatively high localised strain while grains with low Schmid factors were hardly deformed. However, some exceptions (e.g. high strain in lower middle grains) are also found in the test, it is because Schmid factors shown in Fig. 6(e) are calculated based on the assumption of a uniform x-direction tensile stress state in ROI but the local stress state at the grain level is often more complicate [53]. Furthermore, the surface EBSD provides morphology and orientation data for the free surface, but the effects of the sub-surface grains remain unknown.

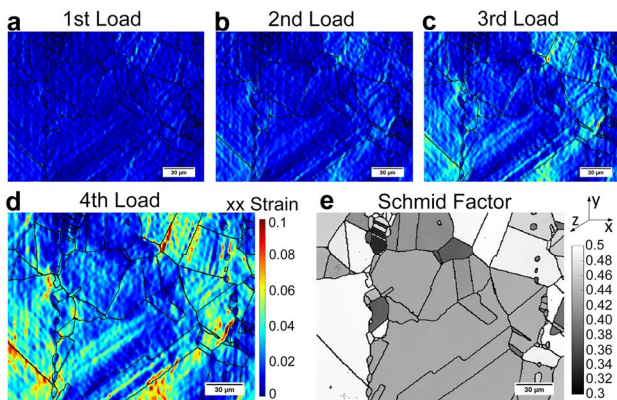


Fig. 6 HR-DIC strain and Schmid factor map of Nitronic 60 sample showing (a–d) ϵ_{xx} map in the ROI (black lines represent grain boundaries), (e) Schmid factor map (loading direction: x-axis)

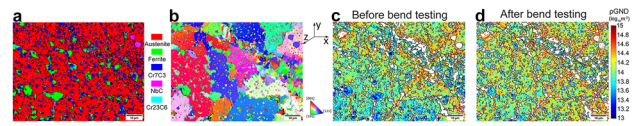


Fig. 7 Results obtained for ROI #1 in Tristelle 5183 sample showing (a) phase map, (b) EBSD orientation maps before test, (c) and (d) HR-EBSD GND density maps before and after bend testing

Tristelle 5183

Iron-based Tristelle 5183 contains more types and higher volume fraction of carbides. This powder metallurgy HIPed material has very small average grain size but some very coarse carbides occurred in its microstructure. HR-EBSD and HR-DIC analyses were carried on one ROI with fine carbides and three ROIs with coarse carbides were selected to compare carbide’s size influence on localized deformation.

According to Fig. 7(a), (b), Tristelle 5183 has a complex microstructure with an average grain size of about $10 \mu\text{m}$. It constitutes of $\sim 70\%$ austenite phase, $\sim 10\%$ ferrite phase and 20% carbides. Carbides mainly grew in the grain boundaries and niobium carbide has the highest proportion among all types of carbides which also has a wider size range. GND density maps are shown in Fig. 7(c), (d) for the austenite and ferrite phases only. Austenite was found to have higher GND density than for ferrite regions before bend testing and GND density significantly increased in both phases showed after test. After test, GND densities were found distributed more homogeneously in all grains which indicates GND’s hardening effect and deformation were prefer to occur in grains with lower GND densities. GND densities did not show very high concentration to grain boundary like Nitronic 60, intragranular carbides probably resulted in this phenomenon. Carbides distributes homogeneously in this ROI, the austenitic/ferritic grains were deformed but carbides still remain the original shape and size which resulted in high GND densities around these carbides across the whole ROI.

As not deformed state Fig. 8(a), (b) show, high residual strains were observed within some grains, thermal expansion mismatch between carbide and austenite during PM-HIP process probably elevated residual stress within these grains. According to Fig. 8(c), (d), unlike high residual strains concentrated at grain boundaries in Nitronic 60 sample, normal/

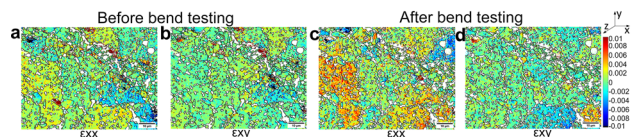


Fig. 8 HR-EBSD elastic residual strain ϵ_{xx} and ϵ_{xy} maps of ROI #1 in Tristelle 5183 sample showing (a) and (b) before bend testing; (c) and (d) after bend testing



shear elastic residual strains in Tristelle 5183 distributed more homogeneously in individual grains. Regions with denser carbides commonly higher residual strains.

According to Tristelle 5183's stress–strain curve, the powder metallurgy HIPing forming route led to a high tensile strength but limited ductility. The heterogeneous strain ϵ_{xx} maps obtained from the HR-DIC measurement are shown in Fig. 9(a)–(d) and the average strain ϵ_{xx} after final cyclic loading is 0.91%. According to strain maps and Schmid factor map, ferritic grains are found have lower strains than austenitic grains even they have similar level of Schmid factors. More persistent slip bands formed while the existed persistent slip bands kept growing after every loading step. High strains commonly located in coarse austenitic grains with high Schmid factors, especially at austenite-carbide phase boundaries. A cluster of fine grains located from central-top to right-middle of ROI are hardly deformed after bend testing, GND density and residual strain in that area were also found lower than other regions. According to Fig. 7(a), (b), this fine grain cluster consist of high fraction of austenitic twins and carbides. Fine grains, twinning and precipitation prohibited slip activation and transfer within the cluster.

As previous mentioned, niobium carbides have a very wide size range and some extreme coarse carbides have considerably detrimental effect on material's mechanical properties. Three Tristelle 5183 samples were tested by the same method as the first sample and three ROIs with coarse carbides were selected to carry out HR-DIC analyses to study these carbides' behaviour in deformation process, results are shown in Fig. 10.

According to Fig. 10(a)–(d), the coarse niobium carbide particle shows no strain within it. The existence of coarse carbide cause heterogeneously distributed strain: grains located at right side of coarse carbide have lower Schmid

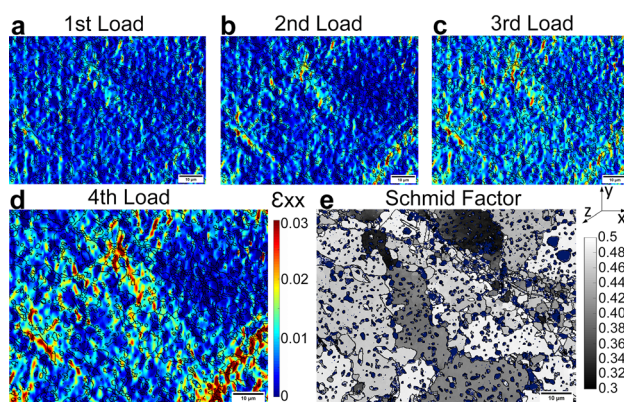


Fig. 9 HR-DIC strain and Schmid factor map of ROI #1 in Tristelle 5183 sample showing (a–d) strain ϵ_{xx} map in the ROI (black lines represent grain boundaries), (e) Schmid factor map of austenite (loading direction: x-axis, blue regions: carbides)

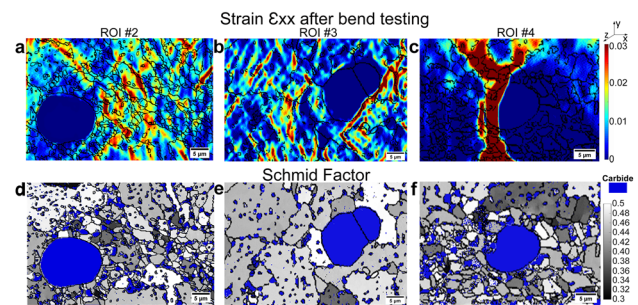


Fig. 10 HR-DIC strain and Schmid factor maps of three ROIs with coarse carbides in Tristelle 5183 samples. (a–c) strain ϵ_{xx} map in the ROI (black lines represent grain boundaries); (d–f) corresponding Schmid factor map of austenite (loading direction: x-axis, blue regions: carbides)

factors but much higher strain ϵ_{xx} than grains above and below the carbide. Similar to the Tristelle 5183 ROI #1, ROI #2 has a cluster of fine grains at the right side of ROI and these fine grains have much lower strains than other coarse grains. As shown in Fig. 10(c)–(e), the coarse carbide is surrounded by some coarse grains with similar levels of Schmid factors. Persistent slip bands formed around the carbide and a high strain developed along the austenite-carbide boundary, it is probable to cause crack initiation and carbide decohesion at this location [54, 55]. For ROI #4, the coarse carbide surrounded by many fine grains directly fractured from its left side after the bend testing and the crack propagated into material's matrix.

Phase distribution and GND density maps of Tristelle 5183 ROI #2 were shown in Fig. 11. GND densities in grains larger than 5 μm were found significantly increased after bend testing while the values in most smaller grains are remained unchanged. The cluster of fine grains in right side of ROI have much lower GND densities than coarser grains adjacent them. Higher GND densities developed at grain boundaries, especially at matrix-carbide boundaries and in large grains with intragranular carbides. After the bend testing, GND density in austenite and ferrite phase increased $10^{13.56} \text{ m}^{-2}$ and $10^{13.47} \text{ m}^{-2}$, respectively.

Figure 12 shows the fracture surface captured from another Tristelle 5183 sample which fractured at applied load of 3500 N. The sample broke into two halves, cracks

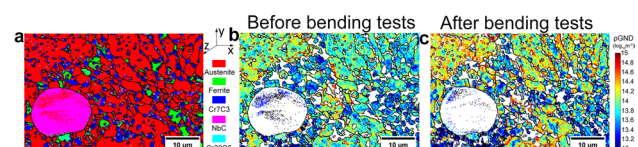


Fig. 11 Results obtained for ROI #2 in Tristelle 5183 sample showing (a) phase map, (b) EBSD orientation maps before test, (c) and (d) HR-EBSD GND density maps before and after bend testing



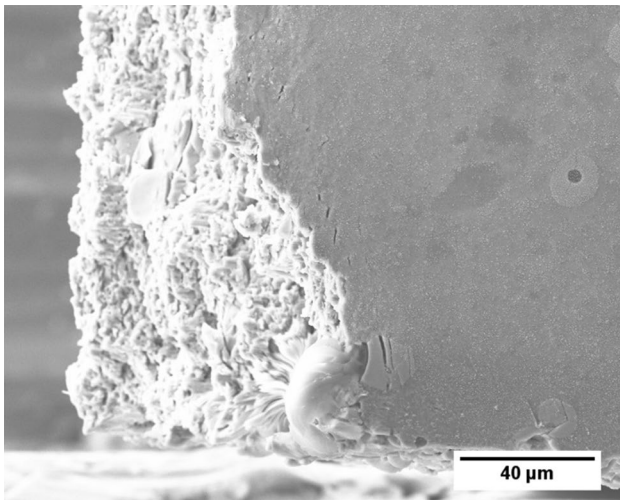


Fig. 12 Fracture surface of a Tristelle 5183 sample

in both carbides and matrix material is observed. A niobium carbide particle with size over 40 μm was found located at the edge of fracture surface, the smooth carbide surface suggests a weak bond between the carbide and matrix which indicates a potential carbide decohesion resulted crack initiation. The sample was polished but only a ~20 μm carbide region was observed in its front surface, it reveals there could be underestimate of carbides' size and effect on deformation of Tristelle 5183.

A brief comparison of EBSD and HR-DIC results are listed in Table 3, the average strain ϵ_{xx} were measured when applied load were removed. Tristelle 5183 has high fraction of carbides while the averaged total strain in it was limited to less than 1% to avoid potential brittle fracture caused by its high carbide contents.

The loading history of the two testing materials are shown in Fig. 13. An obvious yield stress increase can be observed in Nitronic 60 sample and the applied force to cause yield increased more than 300 N after the progressive bend testing. Tristelle 5183 has much higher yield point than Nitronic 60 and there is no clear yield phenomenon observed from its loading history.

Table 3 Phase fractions and average strains after bend testing for the two materials

Material	Phase fractions			Average total strain ϵ_{xx}
	Austenite	Ferrite	Carbides	
Nitronic 60	97%	2.5%	0.5%	3.82%
Tristelle 5183 ROI #1	73.5%	8.3%	18.2%	0.91%
Tristelle 5183 ROI #2	72.1%	8.8%	19.1%	0.93%

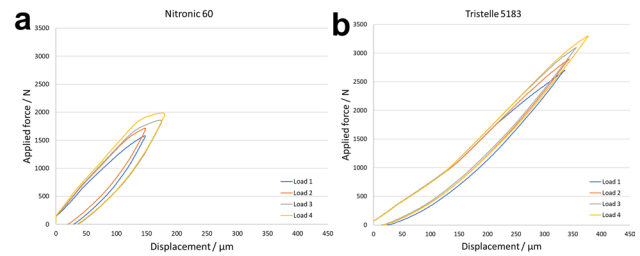


Fig. 13 Bend testing load history of two samples, force–displacement curves were recorded by Zwick Roell mechanical testing machine. (a) Nitronic 60; (b) Tristelle 5183

Discussion

Hough-based EBSD method provides material's phase distribution, grain size and crystal orientation information but the angular resolution is relatively low. HR-EBSD technique uses Kikuchi patterns from conventional EBSD technique to obtain much higher relative angular resolution then gives GND density and residual elastic strain distribution. This technique is helpful to give quantitatively measurement of deformation in micromechanics study, especially for materials with very fine microstructure features. By combing HR-EBSD and HR-DIC methods, samples' elastic and plastic deformation in each phase can be monitored. The acquisition of GND density and residual strain is essential to understand work hardening effect and fracture in different material. Micromechanics test including EBSD, HR-EBSD, HR-DIC and advanced ablation method such as focused ion beam technique can precisely observe deformation in much smaller scales [56, 57]. Dislocations left on the deformed sample by plastic strain worked as constraints to cause lattice curvature in crystalline materials and resulted in an elastic strain region in material, which is also called residual elastic strain. In HR-EBSD correlation process, best quality EBSP in each grain's central area was selected as reference pattern and correlation was carried out with this EBSP to get lattice curvature information. However, there are infinite solutions of GND density for specific lattice curvature, so L_2 -norm minimization method was used to solve the GND density with the minimal total dislocation line length [58, 59]. In calculating residual strain values, HR-EBSD technique is limited to intragranular level due to the reference pattern selection scheme and relative correlation was based on the reference EBSP and relative residual elastic strain was obtained within each grain. The absolute zero strain state is not definable under current methodology [39]. When analysing the HR-EBSD results, GND densities are absolute values but residual elastic strain are relative values which are strongly affected by reference pattern selection. After three-point bend testing, the original reference patterns at the same locations are not obtainable due to the plastic deformation so the elastic



Table 4 Average GND density before and after bend testing

$\log_{10}(\rho_{GND})m^{-2}$	Nitronic 60		Tristelle 5183 ROI #1		Tristelle 5183 ROI #2	
	Austenite	Ferrite	Austenite	Ferrite	Austenite	Ferrite
Before test	13.25	13.46	14.12	13.81	14.02	13.93
After test	13.65	13.97	14.19	13.94	14.15	14.06

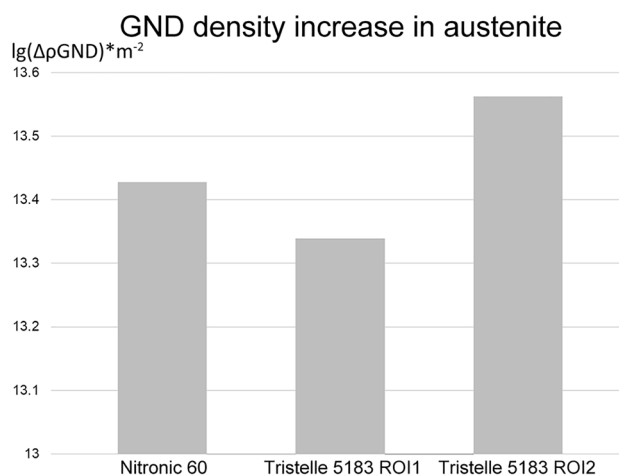
residual strain values cannot simply use after test strain values to subtract before test values.

The forming and heat treatment methods (cast-annealing against PM-HIP) affect materials' mechanical properties significantly. An example is stainless steel Norem 02 (which is a carbide-rich stainless steel similar as Tristelle 5183) formed by PM-HIP method produces finer grains and shorter mean free path between carbides than the cast sample, PM-HIP forming method importantly affect the deformation and enhance material's wear resistance [47]. Nitronic 60 was casted, extruded and annealed cast bar which has a coarse-grain, massive twinning and almost precipitate-free microstructure. As HR-EBSD and HR-DIC results indicated, high fraction of twinning boundaries inhibits slip transfer and accumulate dislocations. Owing to its relatively homogeneous austenitic grain size and lack of precipitates, deformation in this material can be well predicted by Schmid factor calculation. PM-HIPed Tristelle 5183 has much smaller average grain size ($\sim 8 \mu\text{m}$) than Nitronic 60 ($\sim 50 \mu\text{m}$) which enhances its mechanical properties [60]. It also has high volume fraction of carbide which introduces strong precipitate hardening, improves its yield and tensile strength and provides this material exceptional high hardness. Its yield and tensile strength are both 40% higher than that of Nitronic 60 but also has a much lower ductility. The untested PM-HIP formed Tristelle 5183 has high GND density and residual strains at its grain-carbide boundaries which is probably resulted by HIPing process induced thermal expansion mismatch between carbides and matrix. The initial high GND density makes these grains hard to be deformed. High residual elastic strain variations in Tristelle 5183 grains with intragranular carbides also indicates thermal expansion mismatch affected material's microscopic stress state. High GND density regions occurred at grain boundaries, especially at intragranular carbide boundaries which reveals hardening effect of these fine carbides.

GND density in austenite and ferrite are compared in Table 4. GND density in Nitronic 60 dramatically increased due to its 3.82% total strain after test. Ferritic grains are found stiffer than austenitic grains in HR-DIC analysis and average GND densities in Nitronic 60 ferritic grains are also obviously higher than in the austenitic grains. Ferrite fringes made by the extrusion forming process have higher GND densities than the equiaxial austenitic grains even before bend testing. Tristelle 5183 samples have lower average strain which resulted in a slight change of GND density.

Austenite is the major phase in both testing materials, therefore GND density increase in austenite reveal materials'

hardening effect which are compared in Fig. 14. Although very low strain was observed in Tristelle 5183 after tests, its GND density increase is similar as Nitronic 60. When comparing Tristelle 5183 ROI #1 consists mainly fine carbides and ROI #2 with a coarse carbide, average GND density in ROI #2 is much higher than due to the existence of the $\sim 20 \mu\text{m}$ carbide. Strain distribution in Tristelle 5183 can be predicted by Schmid factor but carbides, especially those coarse carbides also have strong influence in its deformation. Extremely coarse carbides shown in Figs. 10, 11 potentially have adverse effects on Tristelle 5183's mechanical properties. Because carbides are not plasticly deformable, austenitic/ferritic grains around the carbides must have higher deformation otherwise carbide decohesion would happen. Therefore, high plastic strain, residual elastic strain and high GND density can be observed around carbides and carbide decohesion would occur the cushion effect from the matrix grains cannot sustain coarse carbides under high strain state. As Fig. 10(a) shows, extremely coarse carbides impose constraints on neighbouring matrix grains so heterogeneous strains were observed in grains around the carbide. High strain developed along austenite-carbide boundary shown in Fig. 10(b) which possibly cause crack initiation at this location and carbide decohesion when higher load was applied. As Fig. 10(c) shows, stress concentration also causes coarse carbide to fracture. Heat treatment to produce material with same carbide fraction but denser fine carbide distribution would dramatically improve material's ductility.

**Fig. 14** GND density change in austenitic grains after bend testing for the two materials

Conclusion

HR-EBSD and HR-DIC quantitative characterisation were utilised on two iron-based alloys undergoing bend testing. Residual elastic strain and GND density were accessed by the HR-EBSD and plastic strain distributions were obtained by HR-DIC. The conclusions based on these investigations are:

- (1) 3.8% and 0.9% total strain ϵ_{xx} was captured by HR-DIC method in Nitronic 60 and Tristelle 5183, respectively. Twinning importantly reinforce Nitronic 60's tensile properties. GND density increases significantly after bending test and GND densities at grain/twin boundaries are commonly higher than that at bulk of grains. Nitronic 60 has high residual elastic strain near some twinning boundaries. Ferrite phase are found harder to be deformed than austenite phase in both testing materials.
- (2) Precipitation strengthening and fine grain strengthening are two important hardening mechanisms in Tristelle 5183. Intragranular carbides resulted in high GND density within the grain before and after tests, which produces a homogeneous GND density increase within the grain, enhances material's yield stress and elevates work hardening rate in this material.
- (3) Extremely coarse carbide results in stress concentration and causes heterogeneous strain distribution. Coarse carbides may have decohesion or fracture and result in the brittle tensile behaviour. For material with same carbide fraction, denser fine carbide distribution would reduce the probability of carbide fracture and decohesion.

Acknowledgements Thanks for the financial support of the National Natural Science Foundation of China (grant numbers 11632010). C. Zhao acknowledge the financial support by the China Scholarship Council (CSC), Rolls-Royce and Imperial College London. C. Zhao want to express thanks to Prof Fionn Dunne, Dr Ben Britton and Dr Jun Jiang for helpful discussions on the experiments.

Declarations

Conflict of Interests The authors have no conflicts of interest to declare that are relevant to the content of this article. The research did not involve any human participants and/or animals.

References

1. Rastogi P (2015) Digital optical measurement techniques and applications. Artech House
2. Li X, Xie H, Kang Y, Wu XJAMSS (2010) A brief review and prospect of experimental solid mechanics in China. 23(6):498–548
3. Sirohi R (2018) Optical methods of measurement: wholefield techniques. CRC Press
4. Wang Q, Ri S, Maenosono A, Tanaka Y, Koyama M (2019) 1-second-resolved strain mapping in Ti-6Al-4V alloys during dwell fatigue in SEM by video sampling moiré. *Mech Mater* 133:63–70
5. Qiu W, Li Q, Lei Z-K, Qin Q-H, Deng W-L (2013) Kang Y-LJC. The use of a carbon nanotube sensor for measuring strain by micro-Raman spectroscopy 53:161–168
6. Ferraro JR (2003) Introductory raman spectroscopy. Elsevier
7. Popov MN, Spitaler J, Veerapandiyar VK, Bousquet E, Hlinka J, Deluca MJnCM (2020) Raman spectra of fine-grained materials from first principles. 6(1):1–7
8. Movasaghi Z, Rehman S, Rehman IUJASR (2007) Raman spectroscopy of biological tissues. 42(5):493–541
9. Dresselhaus MS, Dresselhaus G, Saito R, Jorio AJPr (2005) Raman spectroscopy of carbon nanotubes. 409(2):47–99
10. Malard L, Pimenta MA, Dresselhaus G, Dresselhaus MJPr (2009) Raman spectroscopy in graphene. 473(5–6):51–87
11. Bai Y, Zhang R, Ye X, Zhu Z, Xie H, Shen B, Cai D, Liu B, Zhang C, Jia ZJNn (2018) Carbon nanotube bundles with tensile strength over 80 GPa. 13(7):589–595
12. Li JF, Huang YF, Ding Y, Yang ZL, Li SB, Zhou XS, Fan FR, Zhang W, Zhou ZY, Ren BJn (2010) Shell-isolated nanoparticle-enhanced Raman spectroscopy. 464(7287):392–395
13. Qiu W, Cheng C-L, Liang R-R, Zhao C-W, Lei Z-K, Zhao Y-C, Ma L-L, Xu J, Fang H-J, Kang Y-LJAMS (2016) Measurement of residual stress in a multi-layer semiconductor heterostructure by micro-Raman spectroscopy. 32(5):805–812
14. Stuart BJKOeoc (2000) Infrared spectroscopy
15. Mantsch HH, Chapman D (1996) Infrared spectroscopy of biomolecules. Wiley-Liss New York
16. Qazilbash MM, Brehm M, Chae B-G, Ho P-C, Andreev GO, Kim B-J, Yun SJ, Balatsky A, Maple M, Keilmann FJS (2007) Mott transition in VO₂ revealed by infrared spectroscopy and nano-imaging. 318(5857):1750–1753
17. Barth AJBeBA-B (2007) Infrared spectroscopy of proteins. 1767(9):1073–1101
18. Jiang Z, Henriksen EA, Tung L, Wang Y-J, Schwartz M, Han MY, Kim P, Stormer HLJPr (2007) Infrared spectroscopy of Landau levels of graphene. 98(19):197403
19. Guinier A (1994) X-ray diffraction in crystals, imperfect crystals, and amorphous bodies. Courier Corporation
20. Klug HP, Alexander LE (1974) X-ray diffraction procedures: for polycrystalline and amorphous materials
21. Li Z, Lu C, Xia Z, Zhou Y, Luo ZJC (2007) X-ray diffraction patterns of graphite and turbostratic carbon 45(8):1686–1695
22. Tonouchi MJNp (2007) Cutting-edge terahertz technology. 1(2):97–105
23. Siegel PHJITomt, techniques (2002) Terahertz technology. 50(3):910–928
24. Beard MC, Turner GM, Schmuttenmaer CA (2002) Terahertz spectroscopy. ACS Publications
25. Krivoglaž MA (2012) X-ray and neutron diffraction in nonideal crystals. Springer Science & Business Media
26. Bacon GE (1975) Neutron diffraction. 3
27. Trucano P, Chen RJN (1975) Structure of graphite by neutron diffraction 258(5531):136–137
28. Wenk H, Lutterotti L, Vogel SJPD (2010) Rietveld texture analysis from TOF neutron diffraction data 25(3):283–296
29. Wang Z, Denlinger E, Michaleris P, Stoica AD, Ma D, Beese AMJM, Design (2017) Residual stress mapping in Inconel 625 fabricated through additive manufacturing: Method for neutron diffraction measurements to validate thermomechanical model predictions. 113:169–177



30. Allen A, Hutchings M, Windsor C, Andreani CJ (1985) Neutron diffraction methods for the study of residual stress fields. *J Mater Sci* 34(4):445–473
31. Hutchings MT (2005) Introduction to the characterization of residual stress by neutron diffraction. CRC Press
32. Sunde M, Serpell LC, Bartlam M, Fraser PE, Pepys MB, Blake CCJJ (1997) Common core structure of amyloid fibrils by synchrotron X-ray diffraction. *J Biol Chem* 273(3):729–739
33. Sokolov AA, Ternov IM (1966) Synchrotron radiation
34. Schoenlein R, Chattopadhyay S, Chong H, Glover T, Heimann P, Shank C, Zholents A, Zolotarev MJS (2000) Generation of femtosecond pulses of synchrotron radiation. *Phys Rev Lett* 287(5461):2237–2240
35. Randle V, Engler O (2000) Introduction to texture analysis: microtexture, microtexture and orientation mapping. CRC Press
36. OxfordInstrument. <http://www.ebsd.com/10-ebsd-explained>
37. Wilkinson AJ, Britton TB (2012) Strains, planes, and EBSD in materials science. *Mater Today* 15(9):366–376
38. Schwartz AJ, Kumar M, Adams BL, Field DP (2009) Electron backscatter diffraction in materials science, vol 2. Springer
39. Wilkinson AJ, Meaden G, Dingley DJ (2013) High resolution mapping of strains and rotations using electron backscatter diffraction. *Mater Sci Technol* 22(11):1271–1278. <https://doi.org/10.1179/174328406x130966>
40. Wilkinson AJ, Meaden G, Dingley DJ (2006) High-resolution elastic strain measurement from electron backscatter diffraction patterns: new levels of sensitivity. *Ultramicroscopy* 106(4–5):307–313. <https://doi.org/10.1016/j.ultramicro.2005.10.001>
41. Jiang J, Britton TB, Wilkinson AJ (2012) Accumulation of geometrically necessary dislocations near grain boundaries in deformed copper. *Philos Mag Lett* 92(11):580–588
42. Britton TB, Wilkinson AJ (2012) Stress fields and geometrically necessary dislocation density distributions near the head of a blocked slip band. *Acta Mater* 60(16):5773–5782
43. Kacher J, Landon C, Adams BL, Fullwood D (2009) Bragg's Law diffraction simulations for electron backscatter diffraction analysis. *Ultramicroscopy* 109(9):1148–1156
44. Adams BL, Kacher J (2010) EBSD-based microscopy: Resolution of dislocation density. *Computers, Materials, & Continua* 14(3):185–196
45. Abuzaid W, Sehitoglu H, Lambros J (2013) Plastic strain localization and fatigue micro-crack formation in Hastelloy X. *Mater Sci Eng, A* 561:507–519
46. Yan D, Tasan CC, Raabe D (2015) High resolution in situ mapping of microstrain and microstructure evolution reveals damage resistance criteria in dual phase steels. *Acta Mater* 96:399–409
47. Ocken H (1995) The galling wear resistance of new iron-base hardfacing alloys: a comparison with established cobalt- and nickel-base alloys. *Surf Coat Technol* 76:456–461
48. Sulley J, Stewart D (2016) HIPed Hard Facings for Nuclear Applications: Materials, Key Potential Defects and Mitigating Quality Control Measures. In: 2016 24th International Conference on Nuclear Engineering, 2016. American Society of Mechanical Engineers, pp V001T003A034-V001T003A034
49. Zhao C, Stewart D, Jiang J, Dunne FP (2018) A comparative assessment of iron and cobalt-based hard-facing alloy deformation using HR-EBSD and HR-DIC. *Acta Mater* 159:173–186
50. Cockeram B (2000) Corrosion resistance and electrochemical potentiokinetic reactivation testing of some iron-based hardfacing alloys. *Corrosion* 56(8):849–859
51. Hansen N (2004) Hall-Petch relation and boundary strengthening. *Scripta Mater* 51(8):801–806
52. Pan B, Qian K, Xie H, Asundi A (2009) Two-dimensional digital image correlation for in-plane displacement and strain measurement: a review. *Meas Sci Technol* 20(6):062001
53. Wan V, Cuddihy M, Jiang J, MacLachlan D, Dunne F (2016) An HR-EBSD and computational crystal plasticity investigation of microstructural stress distributions and fatigue hotspots in polycrystalline copper. *Acta Mater* 115:45–57
54. Hunsche A, Neumann P (1986) Quantitative measurement of persistent slip band profiles and crack initiation. *Acta Metall* 34(2):207–217
55. Sangid MD, Maier HJ, Sehitoglu H (2011) A physically based fatigue model for prediction of crack initiation from persistent slip bands in polycrystals. *Acta Mater* 59(1):328–341
56. Wang S, Kalácska S, Maeder X, Michler J, Giuliani F (2019) Britton TBJS. The effect of δ -hydride on the micromechanical deformation of a Zr alloy studied by in situ high angular resolution electron backscatter diffraction. *J Mater Sci* 173:101–105
57. Jun TS, Zhang Z, Dunne FP, Britton TB (2016) Evaluation of Local Rate Sensitivity in a Dwell-Sensitive Ti6242 Using Micropillar Compression. In: Proceedings of the 13th World Conference on Titanium, 2016. Wiley Online Library, pp 498–498
58. Arsenlis A, Parks D (1999) Crystallographic aspects of geometrically-necessary and statistically-stored dislocation density. *Acta Mater* 47(5):1597–1611
59. Kysar J, Saito Y, Oztop M, Lee D, Huh W (2010) Experimental lower bounds on geometrically necessary dislocation density. *Int J Plast* 26(8):1097–1123
60. Hall E (1951) The deformation and ageing of mild steel: III discussion of results. *Proc Phys Soc London, Sect B* 64(9):747

Publisher's Note Springer Nature remains neutral with regard to jurisdictional claims in published maps and institutional affiliations.

